Journal of
Materials Chemistry A

Accepted Manuscript

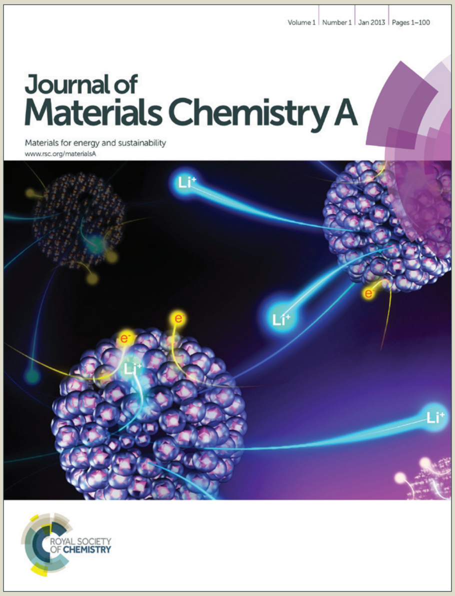

ROYAL SOCIETY OF CHEMISTRY

www.rsc.org/materialsA

Table of contents entry

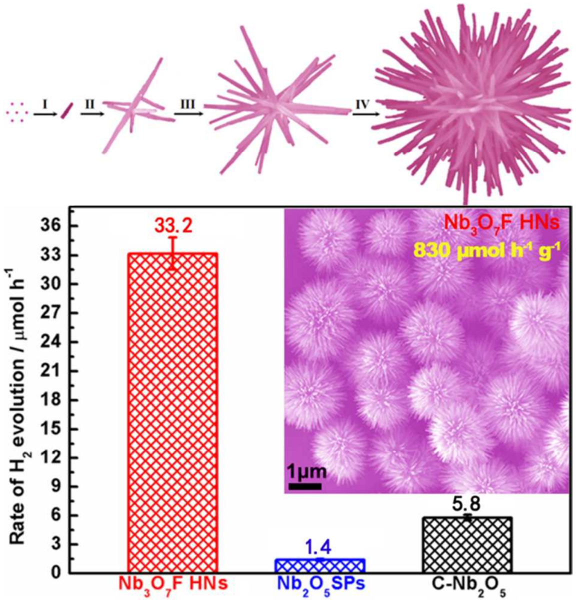

Controllable hydrolysis of H_2NbF_7 with the assistance of 2-propanol can produce Nb_3O_7F hierarchical nanostructures of single-crystalline nanorods for photocatalytic H_2 production.

Cite this: DOI: 10.1039/c0xx00000x

www.rsc.org/xxxxxx

ARTICLE TYPE

Secondary Growth of Hierarchical Nanostructures Only Composed of Nb_3O_7F Single-Crystalline Nanorods as a New Photocatalyst for Hydrogen Production

Junyuan Duan,*[a,b] Guangying Mou,[a] Shuai Zhang,[b] Sheng Wang[b] and Jianguo Guan*[a]

Received (in XXX, XXX) Xth XXXXXXXXX 20XX, Accepted Xth XXXXXXXXX 20XX
DOI: 10.1039/b000000x

Development of efficient photocatalysts for hydrogen (H_2) production from water splitting are highly sought for the current sustainable energy issue. This paper has demonstrated a one-pot hydrothermal approach for the preparation of hierarchical nanostructures (HNs) only composed of Nb_3O_7F single-crystalline nanorods by using H_2NbF_7 as a precursor and 2-propanol as a selective adsorption agent. In our protocol, modulating the hydrolysis rate of coordination complex H_2NbF_7 *via* simply controlling its concentration not only produces Nb_3O_7F single crystalline nanorods by the restrictive growth on [110] due to the selective adsorption of 2-propanol on sidewall, but also create a secondary nucleation for the growth of new nanorods on the pre-formed ones, leading to the formation of the Nb_3O_7F HNs. The resultant Nb_3O_7F HNs strongly response to ultraviolet light and have the band gap of 3.22 eV as well as the conducting band minimum at -0.44 eV. They exhibit an excellent photocatalytic H_2 production activity with a good recycling stability when 0.5 wt% Pt is used as a cocatalyst. The H_2 production rate reaches 830 μmol h^{-1} g^{-1}, about 23.7 and 5.7 times higher than that of the Nb_2O_5 sphere-shaped micro-particles and commercial Nb_2O_5 nanoparticles, respectively. Furthermore, they can also show a notable photocatalytic H_2 production activity even without any cocatalysts. This suggests that the resultant Nb_3O_7F HNs are promising as a new photocatalyst for H_2 production.

Introduction

Photocatlytic hydrogen (H_2) production from water splitting, as a promising and effective approach to obtain renewable solar energy, which may address the growing energy crisis and the related environment pollution concerns, attracts considerable and on-going attentions.[1-4] Designing and exploiting highly-efficient and stable semiconductor photocatalyst is the pivotal issue. Since the landmark discovery of photoelectrochemical water splitting on TiO_2 electrode by Fujishima and Honda,[3] many efforts have been made to attain the target.[5-10] Among them, manufacturing semiconductor photocatalysts at a nanometer scale, which may possess large specific surface areas and abundant surface active sites, has been demonstrated to be one effective route to boost the photocatalytic activities.[11-19] 3D hierarchical nanostructures (HNs) of nanorods, nanowires or nanoplates not only can inherit the full merits of their building blocks but also endow novel characteristics and properties including high structural stability, good recyclability, high porosity, enhanced light scattering and reduced light reflection, etc. Thus some of them with reasonable energy band structures are of significance for water splitting H_2 production.[20-29] Liquid-phase chemical routes are very effective and promising to prepare HNs because of their obvious advantages of low-cost, large-scale production, and easy manipulation.[26, 30-33]

On the other hand, the performances of water splitting H_2 production of photocatalysts are essentially associated with the chemical composition and structures.[34, 35] Semiconductors of Nb-based oxides with d^0 electron configuration have suitable band gaps, more negative conduction band edge than the representative TiO_2, strong oxidizing and reducing power, as well as their non-toxicity and good stability against photo-corrosion and chemical corrosion.[36-55] In this context, a lot of niobium (Nb)-based oxides such as Nb_2O_5, $KNbO_3$, $NaNbO_3$, $Sr_2Nb_2O_7$ and etc, have been developed for photocatalytic H_2 production. In particular, $Nb_3O_7(OH)$ nanorods have recently emerged as a photocatalyst for photocatalytic H_2 production.[56] Nevertheless, to the best of our knowledge, few attentions have so far been paid to the photocatalytic H_2 production of many other documented forms of Nb-based oxides (Nb_3O_7F, NbO_2F and etc),[57-62] even though Nb_3O_7F materials including hierarchical nanostructures have been reported in the application of dye-sensitized solar cells and organic contaminant dye degradation.[60-62] In addition, since the reported Nb_3O_7F HNs contain both large solid cores and nanoplates/nanorod shells, they are obviously adverse to obtain large specific surface area (S_{BET} =13.15 and 35.7 m^2 g^{-1}), and are regarded to have poor photocatlytic performances.[60-63]

Herein, we have developed a one-pot hydrothermal route for the growth of Nb_3O_7F HNs exclusively composed of single-crystalline nanorods as building units by elaborately introducing

H_2NbF_7 as a precursor and 2-propanol as a selective adsorbent. A novel secondary nucleation and growth mechanism of Nb_3O_7F HNs is demonstrated, in which optimizing the hydrolysis rate of H_2NbF_7 via controlling both its concentration and volume ratio of water into 2-propanol not only leads to the spatial constraint growth of Nb_3O_7F nanorods along [001] direction, but also is responsible for the coexistence of the secondary nucleation and subsequent epitaxial growth of new Nb_3O_7F nanorods, resulting in the formation of the resultant Nb_3O_7F HNs. Compared to the previously reported Nb_3O_7F HNs,[60-63] the as-obtained Nb_3O_7F HNs only consist of single crystal nanorods and have a much larger S_{BET} (58.6 m^2 g^{-1}), fitting the photocatalytic H_2 production. Thus, we have for the first time explored the photocatalytic H_2 production from water splitting over the as-obtained Nb_3O_7F HNs, and found that they exhibit excellent photocatalytic H_2 production activities under Xe light irradiation regardless of Pt cocatalysts due to the large S_{BET}, unique hierarchical nanostructures, the thin single crystalline nanorod units, large E_g and rational energy band levels.

Experimentals

Chemical reagents

Niobium pentachloride ($NbCl_5$, 99.9%, AR), 2-Propanol (C_3H_8O, 99.0%, AR), Hydrofluoric acid (HF, 99.6%, AR, 40 wt %), Hydrochloric acid (HCl, AR, 40 wt%), Methanol (99.9%, AR), Hexachloroplatinic acid ($H_2PtCl_6{\bullet}6H_2O$, 99.5%, AR) and commercial Nb_2O_5 particles (C-Nb_2O_5) were all purchased from commercial suppliers and used without further purification. Deionized water (H_2O) was used in all the related reactions.

Synthesis of Nb_3O_7F HNs

Firstly, a colourless transparent solution containing 3.20 g of 40 wt% HF aqueous solution (Notice! HF is highly corrosive and must be manipulated carefully), 0.71 g of $NbCl_5$ powders, 12.40 mL of H_2O and 1.10 mL of 40 wt% HCl aqueous solution, was prepared by magnetically stirring in a plastic bottle and named as S_{Nb}. In a typical synthetic procedure, 1.25 mL of S_{Nb}, 1.25 mL of H_2O and 54.25 mL of 2-propanol were mixed homogeneously and then transferred into a Teflon-lined autoclave with a volume of 100 mL, which was subsequently sealed and heated at 250 ^{o}C for 12 h in an electric furnace. After the autoclave was cooled to room temperature naturally, the white-colour precipitates were separated through centrifugation, washed with ethanol for three times, then dried in a vacuum oven at 60 ^{o}C for 6 h to obtain the resultant Nb_3O_7F HNs samples. To contrast, Nb_3O_7F HNs of different building units were also prepared by changing the volume ratio of 2-propanol and H_2O (R), the concentration of H_2NbF_7 ([H_2NbF_7]), reaction temperature (T) and time (t). The Nb_2O_5 sphere-shaped particles (SPs) were also obtained accordingly by calcining the typical Nb_3O_7F HNs samples in a tube furnace at 800 ^{o}C for 12 h with a heating rate of 12 ^{o}C min^{-1} in air atmosphere.

Characterization

The phase analyses of the samples were detected by the powder X-ray diffraction (XRD; Bruker, D8 Advance), using Cu Kα radiation (λ=1.5418 Å) with a resolution of 0.02^{o} of 2θ from 10^{o} to 80^{o}. The morphologies of the as-synthesized samples were observed by field emission scanning electron microscope (FE-SEM; Hitachi, S-4800, Japan) at 10 kV. The element composition was tested by a Horiba EX250 X-ray energy-dispersive spectrometer (EDX) associated with the FE-SEM. Transmission electron microscopy (TEM) images were captured by the JEOL 2100F high resolution transmission electron microscope at an acceleration voltage of 200 kV (JEOL 2100F, Japan). Ultraviolet-visible absorption spectra of various samples were measured by a UV-Vis spectrophotometer (UV-2550 PC, Shimadzu). The Brunauer–Emmett–Teller (BET) specific surface area (SBET) of the powders was analyzed by nitrogen adsorption in a Micromeritics ASAP 2020 nitrogen adsorption apparatus (USA). All the samples were degassed at 180 ^{o}C prior to nitrogen adsorption measurements. The BET surface area was determined by a multipoint BET method using the adsorption data in the relative pressure (P/P_0) range of 0.05–0.3. The valence band spectrum of the Nb_3O_7F HNs were analyzed using ESCALAB 250Xi X-ray photoelectron spectroscope with a monochromatic Al Kα X-ray source.

Photocatalytic H_2 production activity measurements

The photocatalytic H_2 production activities were measured in a closed gas circulation system with an external-irradiation Pyrex cell, which was placed ~10 cm under a 300 W xenon light (PLS SXE300, Beijing Trusttech Co. Ltd., China) with a average light intensity of 5 mW/cm^2. For the measurements, methanol was employed as the sacrificial reagent. 40 mg of the as-obtained Nb_3O_7F HNs samples loading with 0.5wt% Pt co-catalysts were dispersed in 50 mL of aqueous solution containing 40 vol% methanol. Prior to irradiation, both the reaction cell and the closed gas-circulation system were evacuated. After every 1 h interval of irradiation, 4.23 mL of gases were analyzed in situ with a 7890-II gas chromatograph that equipped with an MS-5A column with a N_2 carrier and a thermal-conductivity detector that was connected to the closed gas-circulating line. 40 mg of Nb_2O_5 SPs and C-Nb_2O_5 samples were selected as a refer to compare the photocatalytic activities. The water-splitting H_2 production activities over 40 mg of Nb_3O_7F HNs of nanorods or nanplates, 40 mg of Nb_2O_5 SPs and 40 mg of C-Nb_2O_5 samples without Pt co-catalyst were also measured.

Results and Discussion

Fig. 1 shows the X-ray diffraction (XRD) pattern of a typical sample obtained after hydrothermal treatment for 12 h. In this pattern, six characteristic diffraction peaks are respectively well indexed to (001), (110), (600), (510), and (111) crystal planes of orthorhombic Nb_3O_7F according to JCPDS card No. 74-2363. No peaks are observed from impurities, indicating that orthorhombic Nb_3O_7F products of high purity are obtained under the present synthetic procedure. Careful comparison of the relative intensities of the six diffraction peaks clearly shows that the intensity of the peak at 2θ = 22.6^{o}, corresponding to plane (001) of Nb_3O_7F, is obviously higher than the others. The calculated ratio between the intensities of the (001) and (110) diffraction peaks is much larger than the normal value (32.41 *versus* 1.36). This suggests that the samples are abundant in (001) crystal planes, and preferentially oriented (or textured) parallel to the surface of the supporting substrate.[64] Meanwhile, some other characteristic diffraction peaks of orthorhombic Nb_3O_7F either are hardly discerned (Fig. S1) or even disappear in the XRD, also suggesting the preferred orientation (or texture) of the sample in XRD test.[64, 65]

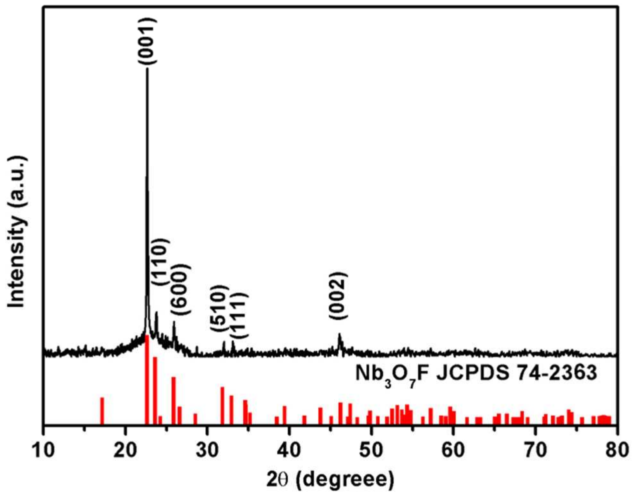

Fig. 1 XRD pattern of the typical Nb_3O_7F HNs.

Scanning electron microscopy (SEM) image (Fig. 2a) demonstrates that the product shows well-dispersed and uniform flower-like hierarchical nanostructures (HNs) with an overall size of about 1.5 μm. No other structure or separated nanorod are discernible from Fig. 2a, illustrating the as-synthesized HNs are of high purity. The high magnification SEM image of a single HN (Fig. 2b) clearly shows that the nanorod units have the average diameters of ~15 nm and lengths of ~700 nm. Close observation of Fig. 2b indicates that all nanorods gradually become a little thin from the centre to both ends, giving a needle-like shape. The transmission electron microscopy (TEM) image (Fig. 2c) further confirms that the as-obtained HNs consist of superbranch nanorods with a uniform diameter of ~15 nm, and all the nanorods exhibit a needle-like shape. No morphological or structural variance after a long time ultrasonication indicates that the HNs are not made up of loosely aggregated nanorods. They are well integrated, and highly stable in surrounding atmosphere. From Figs. 2b and c, it seems that the HNs only contain branched nanorods. As a result, they display an enhanced specific surface area up to 58.6 m^2 g^{-1} (Fig. S2 and Table S1).This is distinctly different from the reported Nb_3O_7F HNs composed of a large solid core in the centre and nanorods with external diameters of ~100 nm (Table S1).[60-63] Fig. 2d shows a high resolution transmission electron microscopy (HRTEM) image of the single nanorod indicated with an arrow in Fig. 2c. The representative interplanar spacing of 0.391 nm is assigned to plane (001) of orthorhombic Nb_3O_7F (JCPDS card No. 74-2363). This, in combination with more HRTEM images taken on the other two single nanorods, evidences the single-crystalline nature and growth direction along [001] of the nanorod units (Fig. S3), well consistent with the result of the XRD pattern (Fig. 1). The above results manifest that the uniform flower-like HNs only composed of hyperbranched Nb_3O_7F single crystal nanorods growing along direction [001] have been successfully prepared by the one-pot hydrothermal route developed here.

It is well known that free Nb^{5+} ions hardly exist in an aqueous solution due to the rapid hydrolysis characteristic, but Nb(V) ions can normally exist in the forms of stable coordination complex such as H_2NbF_7, H_2NbF_6, $NbOF_6^{3-}$ or $NbOF_5^{2-}$ besides oxides or insoluble compounds.[60-62, 66] The underlying chemical reactions during the preparation of the transparent precursor solution (S_{Nb}) may be included as follows.[60-62, 66]

$$NbCl_5 + 7HF \rightarrow H_2NbF_7 + 5HCl \qquad (1)$$

$$NbCl_5 + 6HF \rightarrow HNbF_6 + 5HCl \qquad (2)$$

$$NbCl_5 + 5HF + H_2O \rightarrow H_2NbOF_5 + 5HCl \qquad (3)$$

It is obvious that the Nb(V)-containing precursors generated in S_{Nb} exist as the forms strongly depending on the charged ratio of the content of HF into $NbCl_5$. In our experiment, excess HF are used during the preparation of S_{Nb}. Therefore, the precursors are supposed to be coordination complex H_2NbF_7, which subsequently produces the resultant Nb_3O_7F HNs by a forced hydrolysis according to eqn (4). Herein, HCl is used to adjust the pH and $[H^+]$ of the precursor solution. On one hand, it guarantees the formation of H_2NbF_7 by inhibiting the back reaction of eqn (1). On the other hand, it may adjust the reaction rate of eqn (4) via controlling the concentration of H_2NbF_7.[60-62, 66] In addition, it is able to promote 2-propanol to form an alkoxy group,[67] which will be further discussed in the following parts.

$$3H_2NbF_7 + 7H_2O \rightarrow Nb_3O_7F\downarrow + 20HF \qquad (4)$$

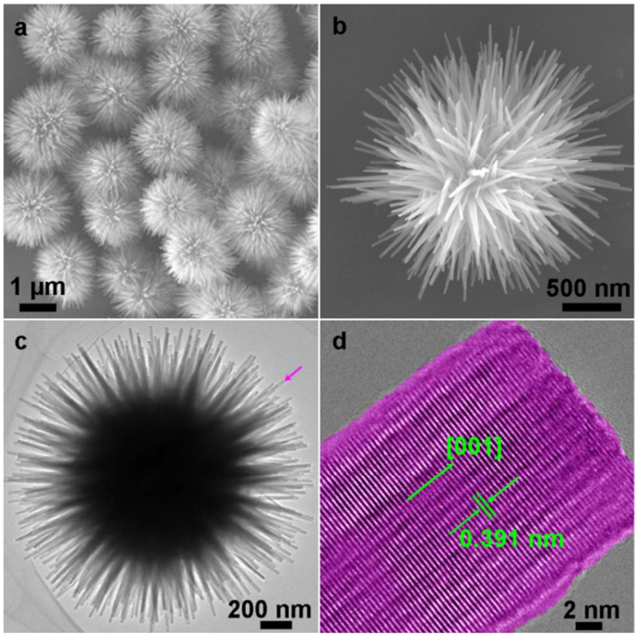

Fig. 2 (a) SEM image of the typical flower-like Nb_3O_7F HNs, (b) high magnification.

In order to understand the growth mechanism of the as-obtained Nb_3O_7F HNs, we have investigated the influences of hydrothermal conditions including the volume ratio of 2-propanol and water (R), the concentration of the precursor H_2NbF_7 ($[H_2NbF_7]$), the hydrothermal temperature (T) and time (t) on the morphologies and structures of the as-obtained products. Fig. 3 shows the SEM images of the as-obtained products at different R. When R is reduced from 56.25 mL/1.25 mL to 50 mL/7.5 mL, the products are still uniform HNs mainly consisting of nanorods as building units, but the overall size becomes 2-3 μm and the diameter of the nanorod units is ~15 nm. Further reducing *R* to 40 mL/17.5 mL also gets uniform HNs with a size of ~2 μm but the building units are evolved into a mixture of nanorods with diameters of ~20 nm and nanoplates with thickness of 50-80 nm and edge lengths of 200-300 nm. When *R* is reduced to 30 mL/27.5 mL, the products are evolved into the HNs of nanoplates (NPs-HNs). The average size of NPs-HNs is ~2 μm. The nanoplate building units are ~100 nm in thickness and ~500 nm in edge length (Figs. 3g-i). At *R* = 0 mL/57.5 mL (without 2-propanol), only the larger HNs (3-4 μm) of smooth nanoplates with ~200 nm in thickness and 3 μm in edge length occur in the products (Figs. 3j-l).

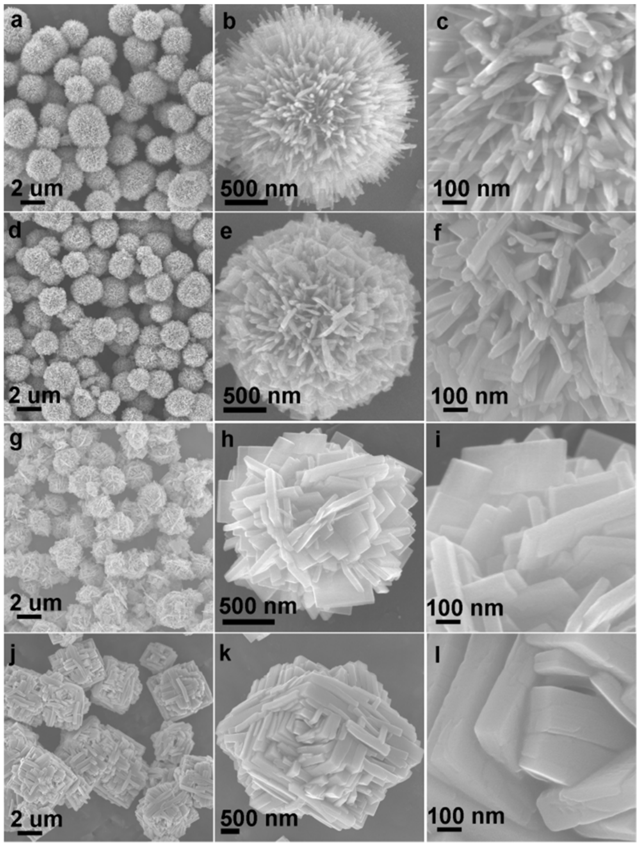

Fig. 3 SEM images of the Nb_3O_7F products obtained at different *R* (the volume ratio of 2-Propanol and water) of (a-c) 50 mL/7.5 mL, (d-f) 40 mL/17.5 mL, (g-i) 30 mL/27.5 mL and (j-l) 0 mL/57.5 mL.

The HNs of Nb_3O_7F nanoplates (Nb_3O_7F NPs-HNs) obtained at *R* = 30 mL/27.5 mL have been deeply characterized by XRD, SEM and TEM. Fig. S4 shows that these NPs-HNs are also in good agreement with orthorhombic phase Nb_3O_7F (JCPDS card No. 74-2363). Compared with Fig. 1, Fig. S4 presents more characteristic diffraction peaks of Nb_3O_7F of orthorhombic phase and an obviously reduced intensity ratio of (001) into (110) planes, suggesting distinct differences in the exposed planes or their relative ratios between the two products. This indicates that *R* has an important influence on the exposed crystal planes of the as-obtained Nb_3O_7F products. SEM images of Nb_3O_7F NPs-HNs show that all the nanoplates grow perpendicularly to each other (Figs. 3g-i and 4a). Fig. 4b reveals that the NPs-HN is a core-free HNs cross-connected with nanoplates and has an external size of ~2 μm. Further observation of Fig. 4b shows the nearly transparent features for both the nanoplates and NPs-HNs, suggesting the relatively thin thickness for the nanoplates and the cross-connect structures shape for the Nb_3O_7F NPs-HNs. Fig. 4c shows the HRTEM image of a single nanoplate taken by the electron beams perpendicular to the surface of the single Nb_3O_7F nanoplate indicated with an arrow in Fig. 4b. The spacing of two perpendicular lattice fringes in the nanoplate are 0.391 nm and 0.376 nm, which correspond to planes (001) and (110) of orthorhombic Nb_3O_7F, respectively. In combination with the selected fast Fourier transform (FFT) image, it illustrates that the nanoplate is a single crystal (Fig. 4d). The above results clearly indicate that *R* has an extremely considerable influence on the morphologies and structures of the products. This is because decreasing *R* will increase the water content, which can obviously modulate the hydrolysis rate of H_2NbF_7 and the subsequent nucleation and growth of Nb_3O_7F crystal. Furthermore, decreasing *R* will also decrease the 2-propanol content. In our protocol, 2-propanol can act as a protective capping agent to control the anisotropic growth of Nb_3O_7F crystal. It tends to heterolytically dissociate into the group $(CH_3)_2CHO^-$ under acidic conditions, which preferentially bounds to the plane (110) of Nb_3O_7F crystals as the plane (110) has a much higher density of unsaturated Nb atoms than the plane (001), restricting the growth of Nb_3O_7F single crystalline nanorods along [110] direction. Consequently, Nb_3O_7F products dominantly grow along [001] direction, forming single crystalline nanorods. This is similar to the truncated bipyramide of TiO_2 single crystals of 64% (001) facets using 2-propanol as capping agents.[67] In a word, simply adjusting *R* can effectively control the nucleation and growth of Nb_3O_7F crystals in the present one-pot hydrothermal route.

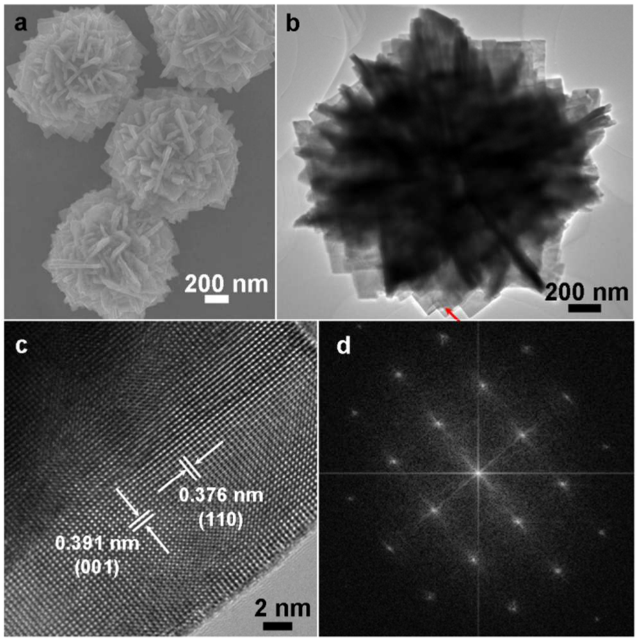

Fig. 4 (a, b) SEM and TEM images of Nb_3O_7F NPs-HNs, (c) the corresponding HRTEM image taken on the nanoplate indicated with an arrow in (b), and (d) the FFT image of (c).

Fig. 5 images a series of the products fabricated at diverse [H_2NbF_7]. Obviously, they are all HNs composed of nanorods, but with slight changes in the external morphologies, as well as the sizes and numbers of the nanorod units. Figs. 5a, d and g indicate that when [H_2NbF_7] is 1.30 mM, the obtained HNs have the sizes of 600 nm. They contain nanorod units of ~20 nm in diameter and 300 nm in length, which are smaller in the diameter, length as well as the average number in each HN. Reducing [H_2NbF_7] definitely decreases the hydrolysis rate of Nb(V) according to eqn (4), and thus reduces the birth, nucleation and growth rate of Nb_3O_7F nanocrystals. In this case, 2-propanol still absorbs on facet (110) to constrain the growth along [110] direction, but the reduced content of the precursor cannot supply enough Nb_3O_7F species to make the nanorods fully grow. Consequently, the diameter and length of the nanorods, as well as the external size of the resultant HNs reduce. In contrast, the HN products obtained at [H_2NbF_7] = 5.85 mM show a size increasing to 3-4 μm, and their building units are evolved into rough nanorods with diameters of ~300 nm and lengths of 1-2 μm (Figs. 5 c, f, i). It can be seen from the end of a single nanorod that it is assembled by the rectangular nanorods through a typical oriented attachment (OA).[68] The increase in the hydrolysis rate of Nb(V) with increasing [H_2NbF_7] would on one hand promote the nucleation and growth rate of Nb_3O_7F crystal concomitantly. On the other hand, it would also accordingly weaken the selective adsorption of 2-propanol on plane (110). Then, the diameter of nanorods, and the overall size of the as-obtained HNs increase certainly, as well as the aspect ratio of nanorods reduces correspondingly. These results and analyses manifest that [H_2NbF_7] have a dominated influences on the morphologies and structures of the building units by changing the nucleation and growth rate of Nb_3O_7F crystals and selective adsorption effect of 2-propanol.

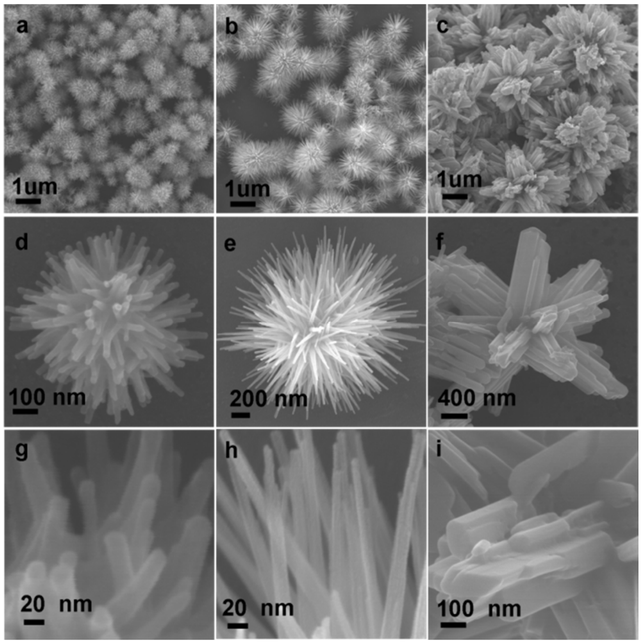

Fig. 5 SEM images of the products obtained at different [H_2NbF_7] of (a, d, g) 1.30 mM, (b, e, h) 3.25 mM and (c, f, i) 5.85 mM.

Fig. 6 shows the SEM images of the products obtained at different *T*. When *T* is reduced from 250 °C to 220 °C, the products are still HNs composed of nanorods. They have an overall sizes of 1.5-2 μm, and the nanorod units have a slightly flattened cross-section, as well as a thin diameter of 10 nm and a length of 700 nm (Fig. 6a). With *T* further reducing to 200 °C, the products still maintain the HNs morphology, but the building units are evolved into nanorods with more flat cross-section (Fig. 6b). Further reducing *T* to 180 °C and 160 °C, the products are evolved into the mixtures of the hyperbranched nanorods and the dispersable nanorods (Figs. 6c-d). Generally, temperature has a strong influence on the nucleation and growth process of crystals. At relatively low temperature (160 and 180 °C), the nucleation and growth rates of Nb_3O_7F are very slow, giving a quasi-equilibrium growth condition due to the constantly low hydrolysis rate of Nb(V) during the overall reaction. Considering the selective adsorption effect of 2-propanol on (110) planes, one dimensional nanorods form as a result from the anisotropic growth. At a relatively high temperature (200, 220 and 250 °C), the enhanced hydrolysis rate of Nb(V) would accelerate the nucleation and growth of Nb_3O_7F crystal accordingly. Nb_3O_7F nanorods form and grow up due to the selective adsorption effect of 2-propanol on (110) planes. As eqn (4) proceeds, the nucleation rate will become far greater than the growth rate. At the same time, strong corrosive HF may etch the sidewall of the pre-formed nanorods due to their higher surface energy, giving some defects on the sidewall.[26, 30-32] As a result, a secondary heterogeneous-nucleation and subsequent epitaxial growth will occur preferentially on the defects of the pre-formed nanorods, finally generating superbranch nanorods and flower-like hierarchical nanostructures by repeating the above described secondary nucleation and epitaxial growth process.

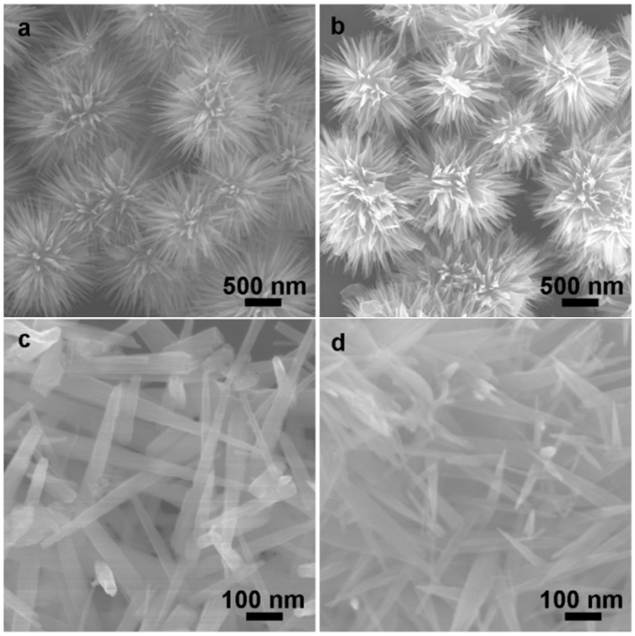

Fig. 6 SEM images of the samples obtained at different *T* of (a) 220 °C, (b) 200 °C, (c) 180 °C, and (d) 160 °C.

In order to decipher morphological and structural evolution of these special Nb_3O_7F HNs, Fig. 7 shows the SEM images of the samples obtained at different *t*. At *t* = 2 h, the obtained HNs consist of nanorods, and have an extremely uneven overall size (Fig. 7a). Besides hyperbranched nanorods in the sample obtained at *t* = 2 h, a few short and small secondary branch nanorods with diameter in ~10 nm and length in 300-400 nm are also noted to grow perpendicularly on the sidewall of the trunk rods (Figs. 7d and g). Prolonging *t* to 12 h, more complex HNs form with 1-1.5 µm in the overall size. Compared with those obtained at *t* = 2 h, the nanorod units in the HNs obtained at *t* = 12 h have similar diameters and morphologies, but their lengths increase to 500 nm and the average number in a single HN increases obviously (Figs. 7b, e and h). Figs. 7e and h imply that the Nb_3O_7F HNs are only composed of more highly hyperbranched nanorods, in which the secondary nanorods grow perpendicularly on the sidewall of the primary rods. These results, in combination with Fig. 2, further prove that the typical Nb_3O_7F HNs are only composed of single crystalline nanorods. At *t* of 24 h, the typical HNs of sizes in 1.5 µm are formed, the diameter, length and average numbers of the nanorod units slightly increase, but the overall dimension doesn't change markedly. In the above reaction stages, no single nanorod has been evidently observed, which is probably attributed to the quick hydrolysis characteristic of the precursor H_2NbF_7. Nevertheless, the dispersable nanorods have been really observed at 160 ^oC and 180 ^oC. The above results and analyses suggest that Nb_3O_7F HNs are generated following a secondary nucleation and subsequent stepwise epitaxial growth mechanism.

As a versatile coordination complex, H_2NbF_7 is much more stable than the Nb^{5+} ions in aqueous solution, and can hydrolyze in a controllable manner by adjusting its concentration, water content and other kinetic parameters. In our protocol, the secondary nucleation and growth of Nb_3O_7F coexists at the overall reaction stage. At the initial reaction stage, the concentration of the species Nb_3O_7F generated by the hydrolysis of H_2NbF_7 is far more than the critical supersaturation degree required for the Nb_3O_7F nucleation. Thus, Nb_3O_7F nuclei forms immediately through homogeneous nucleation, and grow into primary nanorods along [001] due to the selective adsorption effect of 2-propanol on (110) planes. The growth rate of the Nb_3O_7F nanorods will gradually slow down with increasing the nanorod size. In this case, if the species Nb_3O_7F continue to form at a rate bigger than the growth rate, a special secondary heterogeneous-nucleation will take place on the sidewall of the primary nanorods due to the sidewall defects etched by HF, as well as the low energy required by heterogeneous nucleation. Considering the relative small lattice mismatch between planes (001) and (110) (< 4%), and the restricted growth on [110] directions arising from the selective adsorption effect of 2-propanol, the secondary nanorods along [001] grow perpendicularly on the sidewall of the primary nanorods, leading to the formation of the branched nanorods. With the diameter and length of the primary nanorods growing up, the growth rates of the primary nanorods become more and more slowly, and the new-born secondary nanorods grow quickly due to its higher chemical activity and surface energy resulting from smaller sizes. When the formation rate of the species Nb_3O_7F is too slow to maintain the critical concentration for nucleation due to the decrease of $[H_2NbF_7]$ in solution, the crystal growth of Nb_3O_7F will preferentially occur rather than the nucleation. As the reaction time is further prolonged, the diameters and lengths for both the primary and secondary nanorods tend to be the same, and the branch degree of the nanorods increases, generating uniform HNs containing Nb_3O_7F hyperbranched nanorods. The detailed secondary nucleation and growth mechanism is depicted in Scheme 1.

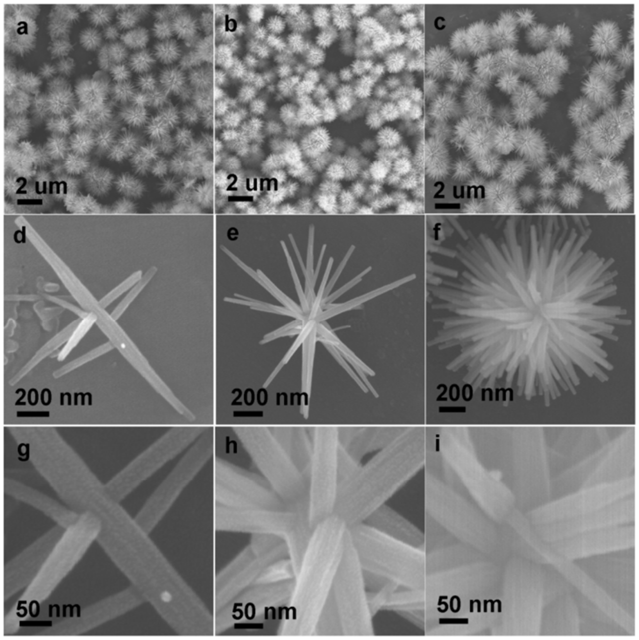

Fig.7 SEM images of the samples obtained at different *t* of (a, d, g) 2 h, (b, e, h) 12 h, (c, f, i) 24 h.

According to the above growth mechanism, the key for the synthesis of these special Nb_3O_7F HNs is to exquisitely use the precursor H_2NbF_7 to manipulate the hydrolysis rate of Nb(V) in the solution, making the formation rate of Nb_3O_7F to match the nucleation and growth rate. In this manner, the secondary heterogeneous-nucleation and subsequent epitaxial growth are created. Rational introduction of 2-propanol induces the restrictive growth on [110] direction, which will effectively control the morphologies and structures of the building units of the HNs. Simply modulating the kinetic parameters including *R*, $[H_2NbF_7]$, *T*, *t* etc can prepare various Nb_3O_7F HNs composed of the controllable building units. Figs. S5-7 clearly show that Nb_3O_7F HNs–NPs also form *via* a same stepwise growth process, further confirming the aforementioned growth mechanism.

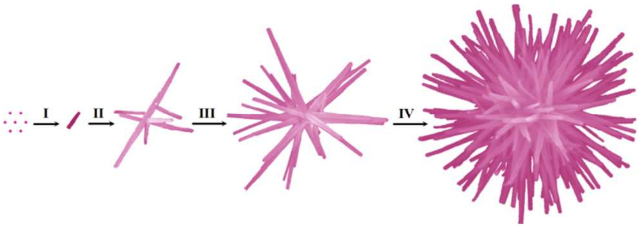

Scheme 1 Schematic illustration of the Nb_3O_7F HNs only consisting of single crystalline nanorods. (I) The spatial constraint growth of Nb_3O_7F species along direction [001] by 2-Propanol absorption on plane (110) leads to the formation of the primary Nb_3O_7F single-crystalline nanorods; (II) secondary nucleation and following epitaxial growth of secondary nanorods along [001] direction on the sidewall defects etched by HF, producing branched nanorods; (III) and (IV) the branching of the nanorods takes place repeatedly with prolonging the reaction time, generating the HNs of Nb_3O_7F hyperbranched nanorods.

The optical properties of the as-prepared Nb_3O_7F HNs have been detected by UV-Vis spectrometer, and compared with the corresponding Nb_2O_5 SPs (Figs. S8 and 9) and the commercial Nb_2O_5 particles (C-Nb_2O_5, Figs. S10 and 11). The UV-Vis absorption spectra clearly show that all the samples exhibit only one steep absorption step at $\lambda< 420$ nm (Fig. 8), suggesting that all of them have a strong absorption in the UV light region. Close observation of the onset of the absorption edge shows that Nb_3O_7F HNs shift to a short wavelength compared with Nb_2O_5 SPs and C-Nb_2O_5. According to Kubelka–Munk function, the bandgap energy (E_g) for semiconductors can be simply estimated from a plot of $(A/\lambda)^{1/2}$ versus $1240/\lambda$, where A is absorbance, and λ is the associated wavelength. The estimated E_g of Nb_3O_7F HNs, Nb_2O_5 SPs and C-Nb_2O_5 are about 3.22 eV, 2.93 eV and 3.05 eV respectively (The inset of Fig. 8), indicating that Nb_3O_7F HNs and C-Nb_2O_5 can only absorb UV light, while Nb_2O_5 SPs may absorb some visible light at $\lambda \leq 423$ nm. No F element is observed in the EDX spectrum of Nb_2O_5 SPs (Fig. S9). This, in combination with the Figs. S8-11, illustrates that the difference of E_g between Nb_2O_5 SPs and C-Nb_2O_5 probably arises from the difference in crystal structure, as reported in the TiO_2 photocatalyst.[69-73] The Nb_3O_7F HNs exhibit the slightly larger E_g than both Nb_2O_5 SPs and C-Nb_2O_5 due to the differences in the chemical compositions and structures (Figs. S7-8, S11-12).

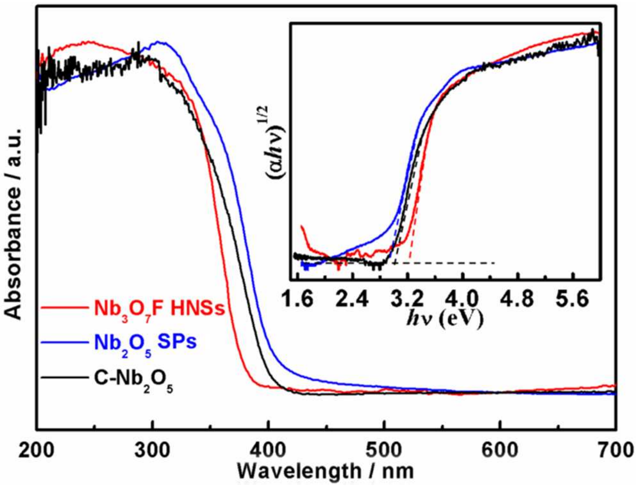

Fig. 8 UV-Vis absorption spectra of Nb_3O_7F HNs, Nb_2O_5 SPs and C-Nb_2O_5 samples.

To understand the electronic structure of the Nb_3O_7F HNs, density functional theory (DFT) calculations and X-ray photoelectron spectroscopy (XPS) measurements of the valence-band spectrum were carried out. Fig. S13 clearly shows that their conduction band (CB) is composed of Nb 4d orbits and their valence band (VB) is composed of Nb 5p, O 2p and F 2p orbits together. This further illustrates that the differences in E_g among the Nb_3O_7F HNs, Nb_2O_5 SPs and C-Nb_2O_5 are derived from the difference in the chemical composition and structures. The band gap (E_g) of the Nb_3O_7F HNs is calculated to be ca.1.83 eV, 1.39 eV smaller than the experimental value (3.22 eV) as a result of the well-known band gap under estimation within the framework of standard DFT.[74] The energies of the VB maximum (VBM) and the CB minimum (CBM) intrinsically determine the oxidation and reduction potentials of photo-generated holes and electrons in photocatalytic reactions. The VBM of Nb_3O_7F HNs is determined to be 2.78 eV from Fig. S14.[74-75] By combining this result with Fig. 8, the CBM of the Nb_3O_7F HNs is calculated to be -0.44 eV and thus the band structure of the Nb_3O_7F HNs could be also determined (Fig. S15). The above results suggest that the Nb_3O_7F HNs are suitable for photocatalytic water splitting.

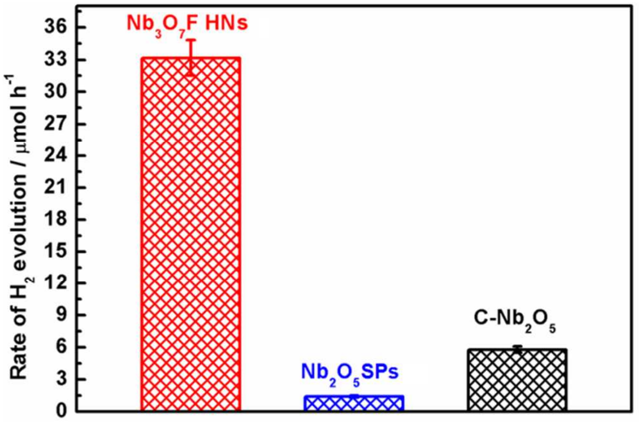

Fig. 9 Comparisons of photocatalytic H_2 production activities from 50 mL of aqueous solution containing 40 vol% methanol over 40 mg of Nb_3O_7F HNs, Nb_2O_5 SNPs and C-Nb_2O_5 loaded with 0.5wt% Pt under Xe light irradiation.

In order to evaluate the photocatalytic activity, 40 mg of Nb_3O_7F HNs loaded with 0.5 wt% Pt were dispersed in 50 mL of aqueous solution containing 40 vol% methanol, and irradiated under 300 W Xe light. For comparison, photocatalytic H_2 production performances over 40 mg of Nb_2O_5 SPs and C-Nb_2O_5 were also tested. As shown in Fig. 9, Nb_3O_7F HNs, Nb_2O_5 SPs and C-Nb_2O_5 exhibit photocatalytic H_2 production rates of 33.2, 1.4 and 5.8 μmol h^{-1}, respectively, or of 830, 35 and 145 μmol h^{-1} g^{-1}, respectively. Nb_3O_7F HNs exhibit more excellent photocatalytic H_2 production activities than both Nb_2O_5 SPs and C-Nb_2O_5. Their photocatalytic H_2 production rate of the Nb_3O_7F HNs is about 23.7 and 5.7 times higher than that of Nb_2O_5 SPs and C-Nb_2O_5, respectively. No H_2 gas is detected without irradiation or the photocatalysts, suggesting that the H_2 production comes from the photocatalytic reaction over the Nb_3O_7F HNs samples. The enhancement of the photocatalytic activities may be reasonably attributed to the following four factors: (i) the Nb_3O_7F HNs have a large surface area (Table S2), which can provide more surface active sites for the adsorption of reactant molecules, making the photocatalytic process more efficient. (ii) The unique characteristics of the HNs structures are believed to facilitate the transportation of reactants and products through the interior space due to the interconnected porous network, and favor the harvesting of exciting light due to the enlarged surface area and multiple scattering within the porous framework. They can also effectively prevent the agglomeration of photocatalysts. (iii) The single-crystalline nanorod structures possess few defects, where photogenerated electrons and holes may recombine. In addition, the small diameter of nanorod units can shorten the migration path of the photogenerated electrons, reducing their recombination rate inside. (iv) The Nb_3O_7F HNs show lager E_g, and thus the photo-excited electrons in Nb_3O_7F HNs possess a strong reducing ability for photocatalytic reaction of H^+ (Fig. 8).

The photocatalytic stability of the Nb_3O_7F HNs loaded with 0.5 wt% Pt under Xe light irradiation has also been tested. The photocatalyst were separated by centrifugation and renewedly dispersed in 50 mL of aqueous solution containing 40 vol% methanol after every 10 hours. Fig. 10 displays the typical time courses for H_2 evolution over the Nb_3O_7F HN samples. As presented from a single cycle, the amount of H_2 evolution grows linearly with the irradiation time, suggesting the almost constant H_2 evolution activities. As displayed in Fig. 10, the phocatalytic activity has no noticeable decrease after 5 cycles, demonstrating a good stability of the Nb_3O_7F HNs for photocatalytic H_2 production from water splitting by employing methanol as sacrificial agent under Xe light irradiation.

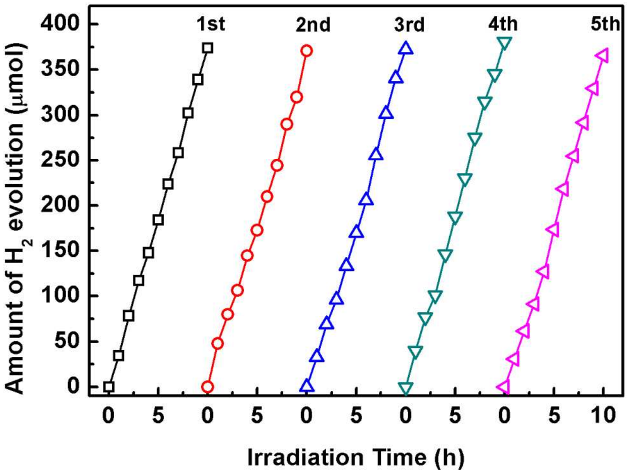

Fig. 10 The long-term photocatalytic H_2 production stability over 40 mg of Nb_3O_7F HNs loaded with 0.5 wt% Pt under Xe light irradiation.

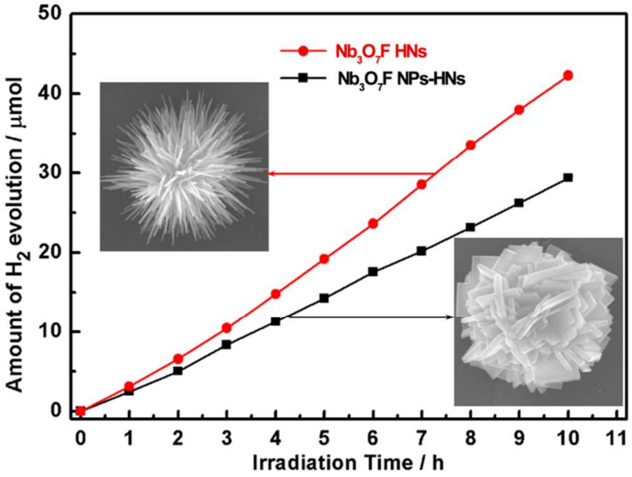

Fig. 11 Comparisons of photocatalytic H_2-production activities for 40 mg of Nb_3O_7F HNs and NPs-HNs without co-catalysts from 50 mL of aqueous solution containing 40 vol% methanol under Xe light irradiation.

Usually, single photocatlytic materials exhibit poor photocatalytic activity for H_2 production and even no activity due to the quick recombination of photogenerated charge carriers before their migrating to the surface for reactions. Therefore, the cocatalysts such as Pt are necessarily used. Fig. 11 indicates that both of the Nb_3O_7F HNs exhibit some notable photocatalytic activities. The H_2 production rate is 4.2 and 2.9 μmol h^{-1}, respectively. In contrast, no H_2 gas is detected over the Nb_2O_5 SPs and the C-Nb_2O_5 samples, suggesting the quick recombination of photo-excited electrons and holes in them. This result indicates that the Nb_3O_7F HNs have excellent photocatalytic ability for water splitting H_2 production. Because the HNs of Nb_3O_7F nanorods have a lager special surface area, they exhibit about 0.45 times higher photocatalytic H_2 production activities than the HNs of Nb_3O_7F nanoplates (Table S2). The above results and discussion suggests a new efficient and stable Nb_3O_7F HNs photocatalyst for H_2 production from water splitting.

Conclusions

In summary, we have demonstrated a facile one-pot hydrothermal approach for the large-scale preparation of flower-like Nb_3O_7F HNs only composed of single nanorods by using H_2NbF_7 as a precursor, 2-propanol as a selective adsorption agent and HCl as a pH-regulating agent. In this protocol, exquisitely controlling the hydrolysis rate of the precursor H_2NbF_7 not only can generate Nb_3O_7F single crystalline nanorods via the restrictive growth on [110] of Nb_3O_7F due to the selective adsorption of 2-propanol on sidewalls, but also can induce a novel secondary nucleation and subsequent epitaxial growth of the newly formed Nb_3O_7F on the primary nanorod surfaces due to the reduced growth rate, sidewall defects etched by HF and the low mismatching lattices between (001) and (110) faces, resulting in the formation of Nb_3O_7F HNs. It is believed that this synthetic strategy can be extended for the fabrication of hierarchical nanostructures of other metallic oxides, such as Ta_2O_5 or Ta_3O_7F. Furthermore, the as-obtained Nb_3O_7F HNs exhibit much more excellent photocatalytic water splitting H_2 production activities than the C-Nb_2O_5 and Nb_2O_5 SPs regardless of Pt cocatalyst, due to large surface area, unique hierarchical nanostuctures and large Eg. When 0.5 wt% Pt is employed as a cocatalyst, the Nb_3O_7F HNs show a photocatalytic H_2 production rate as high as 830 μmol h^{-1} g^{-1}, about 23.7 and 5.7 times higher than that of C-Nb_2O_5 and Nb_2O_5 SPs, respectively, and a good photocatalytic stability. In addition to their promising application as an efficient photocatalyst for water splitting H_2 prodution, the above Nb_3O_7F HNs are also expected to have potential applications in the fields of photocatalytic degradation of organic pollutants and dye-sensitized solar cells.

Acknowledgements

This work financially was supported by the National Natural Science Foundation of China (51002111 and 51303144) and the Top Talents Lead Cultivation Project of Hubei Province. This work was also partly supported by the Youth Scientific Research Fund of Qinghai University (2014-QGY-9) and the Fundamental Research Funds for the Midwest Universities (QHJ-2013-02).

Notes and references

[a] *State Key Laboratory of Advanced Technology for Materials Synthesis and Processing, Wuhan University of Technology, 122 Luoshi Road, Wuhan 430070, China. Fax: 86 27 87218832; Tel: 86 27 87218832; E-mail: guanjg@whut.edu.cn*

[b] *Qinghai Provincial Key Laboratory of New Light Alloys, School of Mechanical Engineering, Qinghai University, 251 Ningda Road, Xining 810016, China. Fax: 86 971 5310440; Tel: 86 971 5168415; E-mail: junyuanduan@sina.com*

† Electronic Supplementary Information (ESI) available: Nitrogen adsorption–desorption isotherm of Nb_3O_7F, HRTEM images of Nb_3O_7F nanorods; XRD patterns of Nb_3O_7F NPs-HNs, Nb_2O_5 SPs and C-Nb_2O_5;

SEM images of Nb_3O_7F NPs-HNs obtained at different C_p, T and t, Table of the S_{BET} comparision of various samples; EDX pattern of Nb_2O_5 SPs; SEM images of Nb_2O_5 SPs and C-Nb_2O_5 samples, caclcuated band structure and DOS images, band structure diagram. See DOI: 10.1039/b000000x/

1 M. D. Karkas, E. V. Johnston, O. Verho and B. Akermark, Acc. Chem. Res., 2014, 47, 100-111.
2. Y. Tachibana, L. Vayssieres and J. R. Durrant, Nat. Photonics, 2012, 6, 511-518.
3. A. Fujishima and K. Honda, Nature, 1972, 238, 37-38.
4. E. A. Chandross, Science, 2014, 344, 469-469.
5. T. Hisatomi, J. Kubota and K. Domen, Chem. Soc. Rev., 2014, 43, 7520-7535.
6. A. Mukherji, R. Marschall, A. Tanksale, C. Sun, S. C. Smith, G. Q. Lu and L. Wang, Adv. Func. Mater., 2011, 21, 126-132.
7. Z. H. Liu, Z. Z. Lou, Z. J. Li, G. Wang, Z. Y. Wang, Y. Y. Liu, B. B. Huang, S. Q. Xia, X. Y. Qin, X. Y. Zhang and Y. Dai, Chem. Comm., 2014, 50, 11046-11048.
8. D. J. Martin, P. J. T. Reardon, S. J. A. Moniz and J. Tang, J. Amer. Chem. Soc., 2014, 136, 12568-12571.
9. M. Yashima, H. Yamada, K. Maeda and K. Domen, Chem. Comm., 2010, 46, 2379-2381.
10. K. Maeda and K. Domen, Chem. Mater., 2010, 22, 612-623.
11. L. Liao, Q. H. Zhang, Z. H. Su, Z. Z. Zhao, Y. N. Wang, Y. Li, X. X. Lu, D. G. Wei, G. X. Feng, Q. K. Yu, X. J. Cai, J. M. Zhao, Z. F. Ren, H. Fang, F. Robles-Hernandez, S. Baldelli and J. M. Bao, Nat. Nanotechol., 2014, 9, 69-73.
12. N. Thanh-Dinh, D. Cao-Thang and D. Trong-On, Chem. Comm., 2015, 51, 624-635.
13. J. Q. Wang, S. Y. Su, B. Liu, M. H. Cao and C. W. Hu, Chem. Comm., 2013, 49, 7830-7832.
14. F. E. Osterloh, Chem. Soc. Rev., 2013, 42, 2294-2320.
15. X. B. Ge, L. Y. Chen, L. Zhang, Y. R. Wen, A. Hirata and M. W. Chen, Adv. Mater., 2014, 26, 3100-3104.
16. S. Rawalekar and T. Mokari, Adv. Energy Mater., 2013, 3, 12-27.
17. L. L. Xu, J. G. Guan and W. D. Shi, ChemCatChem, 2012, 4, 1353-1359.
18. C. Tao, L. L. Xu and J. G. Guan, Chem. Eng. J., 2013, 229, 371-377.
19. L. K. Li, L. L. Xu, W. D. Shi and J. G. Guan, Int. J. Hydrogen Energ., 2013, 38, 816-822.
20. L. Zhang, H. B. Wu, Y. Yan, X. Wang and X. W. Lou, Energ. Environ. Sci., 2014, 7, 3302-3306.
21. M. F. Shao, F. Y. Ning, M. Wei, D. G. Evans and X. Duan, Adv. Func. Mater., 2014, 24, 580-586.
22. S. Y. Noh, K. Sun, C. Choi, M. Niu, M. Yang, K. Xu, S. Jin and D. Wang, Nano Energy, 2013, 2, 351-360.
23. C. W. Cheng and H. J. Fan, Nano Today, 2012, 7, 327-343.
24. W. D.Shi, J. Q. Shi, S. Yu and P. Liu, Appl. Catal. B-Environ., 2013, 138, 184-190.
25. Y. X. Li, G. Chen, Q. Wang, X. Wang, A. K. Zhou and Z. Y. Shen, Adv. Func. Mater., 2010, 20, 3390-3398.
26. J. Y. Duan, W. D. Shi, L. L. Xu, G. Y.Mou, Q. L. Xin and J. G. Guan, Chem. Comm., 2012, 48, 7301-7303.
27. M. J. Bierman and S. Jin, Energ. Environ. Sci., 2009, 2, 1050-1059.
28. L. Shang, C. Zhou, T. Bian, H. J. Yu, L. Z. Wu, C. H. Tung and T. R. Zhang, J. Mater. Chem. A, 2013, 1, 4552-4558.
29. J. X. Zhu, Z. Y. Yin, D. Yang, T. Sun, H. Yu, H. E. Hoster, H. H. Hng, H. Zhang and Q. Y. Yan, Energ. Environ. Sci., 2013, 6, 987-993.
30. T. L. Sounart, J. Liu, J. A. Voigt, J. W. P. Hsu, E. D. Spoerke, Z. Tian and Y. B. Jiang, Adv. Func. Mater., 2006, 16, 335-344.
31. T. L. Sounart, J. Liu, J. A. Voigt, M. Huo, E. D. Spoerke and B. McKenzie, J. Amer. Chem. Soc., 2007, 129, 15786-15793.
32. T. Zhang, W. Dong, M. Keeter-Brewer, S. Konar, R. N. Njabon and Z. R. Tian, J. Amer. Chem. Soc., 2006, 128, 10960-10968.
33. F. Z. Mou, J. G. Guan, Z. D. Xiao, Z. G. Sun, W. Shi and X. A. Fan, J. Mater. Chem., 2011, 21, 5414-5421.
34. X. B. Chen, S. H. Shen, L. J. Guo and S. S. Mao, Chem. Rev., 2010, 110, 6503-6570.
35. A. Kudo and Y. Miseki, Chem. Soc. Rev., 2009, 38, 253-278.
36. H. Luo, W. Song, P. G. Hoertz, K. Hanson, R. Ghosh, S. Rangan, M. K. Brennaman, J. J. Concepcion, R. A. Binstead, R. A. Bartynski, R. Lopez and T. J. Meyer, Chem. Mater., 2013, 25, 122-131.
37. H. Y. Lin, H. C. Yang and W. L. Wang, Catal. Today, 2011, 174, 106-113.
38. X. Chen, T. Yu, X. Fan, H. Zhang, Z. S. Li, J. H.Ye and Z. G. Zou, Appl. Surf. Sci., 2007, 253, 8500-8506.
39. Y. H. Pai and S. Y. Fang, J. Power Sources, 2013, 230, 321-326.
40. S. X. Ge, H. M. Jia, H. X. Zhao, Z. Zheng and L. Z. Zhang, J. Mater. Chem., 2010, 20, 3052-3058.
41. D. Chen and J. H. Ye, Chem. Mater., 2009, 21, 2327-2333.
42. Y. Hosogi, Y. Shimodaira, H. Kato, H. Kobayashi and A. Kudo, Chem. Mater., 2008, 20, 1299-1307.
43. Y. F. Huang, Y. L. Wei, L. Q. Fan, M. L. Huang, J. M. Lin and J. H. Wu, Int. J. Hydrogen Energ., 2009, 34, 5318-5325.
44. Y. X. Li, G. Chen, H. J. Zhang and Z. S. Lv, Int. J. Hydrogen Energ., 2010, 35, 2652-2656.
45. H. Y. Lin, T. H. Lee and C. Y. Sie, Int. J. Hydrogen Energ., 2008, 33, 4055-4063.
46. Y. F. Huang, J. Li, Y. L. Wei, Y. B. Li, J. M. Lin and J. H. Wu, J. Hazard Mater., 2009, 166, 103-108.
47. B. D. Alexander, P. J. Kulesza, L. Rutkowska, R. Solarska and J. Augustynski, J. Mater. Chem., 2008, 18, 2298-2303.
48. J. Choi, S. Y. Ryu, W. Balcerski, T. K. Lee and M. R. Hoffmann, J. Mater. Chem., 2008, 18, 2371-2378.
49. R. Abe, M. Higashi, K. Sayama, Y. Abe and H. Sugihara, J. Phys. Chem. B, 2006, 110, 2219-2226.
50. H. Kato, H. Kobayashi and A. Kudo, J. Phys. Chem. B, 2002, 106, 12441-12447.
51. A. Kudo, H. Kato and S. Nakagawa, J. Phys. Chem. B, 2000, 104, 571-575.
52. Q. P. Ding, Y. P. Yuan, X. Xiong, R. P. Li, H. B. Huang, Z. S. Li, T. Yu, Z. G. Zou and S. G. Yang, J. Phys. Chem. C, 2008, 112, 18846-18848.
53. P. V. Kamat, J. Phys. Chem. C, 2007, 111, 2834-2860.
54. X. Li and J. H. Ye, J. Phys. Chem. C, 2007, 111, 13109-13116.
55. J. Lv, T. Kako, Z. S. Li, Z. G. Zou and J. H. Ye, J. Phys. Chem. C, 2010, 114, 6157-6162.
56. M. Hmadeh, V. Hoepfner, E. Larios, K. Liao, J. Jia, M. Jose-Yacaman and G. A. Ozin, ChemSusChem, 2014, 7, 2104-2109.
57. S. Andersson, Acta Chemica Scandinavica 1964, 18, 2339-2344.
58. T. Murase, H. Irie and K. Hashimoto, J. Phys. Chem. B, 2005, 109, 13420-13423.
59. M. V. Reddy, S. Madhavi, G. V. S. Rao and B. V. R. Chowdari, J. Power Sources, 2006, 162, 1312-1321.
60. Z. Wang, J. G. Hou, C. Yang, S. Q. Jiao, K. Huang and H. M. Zhu, Phys. Chem. Chem. Phys., 2013, 15, 3249-3255.
61. H. M. Zhang, Y. B. Li, Y. Wang, P. R. Liu, H. G. Yang, X. D. Yao, T. C. An, B. J. Wood and H. J. Zhao, J. Mater. Chem. A, 2013, 1, 6563-6571.
62. F. Idrees, C. Cao, F. K. Butt, M. Tahir, M. Tanveer, I. Aslam, Z. Ali, T. Mahmood and J. Hou, CrystEngComm, 2013, 15, 8146-8152.
63. F. Huang, Z. Y. Fu, W. M. Wang, H. Wang, Y. C. Wang, J. Y. Zhang, Q. J. Zhang, S. W. Lee and K. Niihara, Mater. Res. Bull., 2010, 45, 739-743.
64. Y. G. Sun and Y. N. Xia, Science, 2002, 298, 2176-2179.
65. L.Vayssieres, Adv. Mater. 2003,15,464-466.
66. I. M. Gibalo, Analytical Chemistry of Niobium & Tantalum, ANN Arbor-Humphey Sci. Pubilishers, Inc., London, 1970..
67. H. G. Yang, G. Liu, S. Z. Qiao, C. H. Sun, Y. G. Jin, S. C. Smith, J. Zou, H. M. Cheng and G. Q. Lu, J. Amer. Chem. Soc., 2009, 131, 4078-4083.
68. Q. Zhang, S. J. Liu and S. H. Yu, J. Mater. Chem., 2009, 19, 191-207.
69. L. Liu, H. Zhao, J. M. Andino and Y. Li, ACS Catal., 2012, 2, 1817-1828.
70. M. Addamo, M. Bellardita, A. Di Paola and L. Palmisano, Chem. Comm., 2006, 47, 4943-4945.
71. D. Dambournet, I. Belharouak and K. Amine, Chem. Mater., 2010, 22, 1173-1179.

72. Y. L. Liao, W. X. Que, Q. Y. Jia, Y. C. He, J. Zhang and P. Zhong, J. Mater. Chem., 2012, 22, 7937-7944.
73. J. Schneider, M. Matsuoka, M. Takeuchi, J. Zhang, Y. Horiuchi, M. Anpo and D. W. Bahnemann, Chem.Rev., 2014, 114, 9919-9986.
74. G. Liu, P. Niu, L. C. Yin and H. M. Cheng, J. Am. Chem. Soc. 2012, 134, 9070−9073.
75. X. B. Chen, L. Liu, P. Y. Yu and S. S. Mao. Sience, 2011, 331,746-750.